Food & Health 2025, 8(2): 1-11

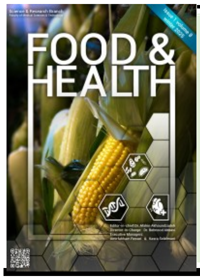

Food & Health Journal

Journal homepage: sanad.iau.ir/journal/fh

Optimization and measure scatter ratio by Robust Fourier-based slanted-edge method

Mehdi Fazli *[1]

[1] Department of Mathematics, Ardabil Branch, Islamic Azad University, Ardabil, Iran.

ARTICLE INFO

Original Article

Article history:
Received 29 January 2025
Revised 17 February 2025
Accepted 10 March 2025
Available online 25 March 2025

Keywords:
Fourier domain
X-ray imaging
X-ray scatter
Optimization

ABSTRACT

Patient scatter incident on an x-ray detector reduces radiographic contrast and adds quantum noise, and minimizing scatter is critical in some specialized techniques such as dual-energy and energy-subtraction methods. Existing methods to measure scatter are either labor-intensive ‘(multiple disks) or not appropriate to use in radiography where scatter often exceeds the width of the x-ray beam. Develop a method to measure the scatter-to-primary ratio (SPR) that can be used for a wide range of radiographic and mammographic conditions, both with scatter equilibrium (scatter function does not exceed primary-beam width) and without. Fourier theory is used to show the SPR can be measured from the low-frequency drop (LFD) of the Fourier transform of the derivative of a nor- malized edge profile. The method was validated both experimentally and by simulation for radiography and mammography under scatter equilibrium and nonequilibrium conditions. The theoretical derivation showed that by normalizing an edge profile with a profile without the edge, scatter equilibrium is not required and the method accommodates a nonuniform primary beam from beam divergence and Heel effect. The method was validated by a simulation study for a range of scatter-LSF’ widths, primary-beam widths, and image regions of interest used in the analysis. Experimental scatter measurements agreed with a similar edge-method published by Cooper when scatter equilibrium is achieved.

1. Introduction

X-Ray scatter generated within a patient reduces radiographic contrast by adding a near-uniform scatter signal to the image and reduces signal-to-noise ratio (SNR) by adding quantum (Poisson) noise from detection of scatter photons (1). Scatter is often minimized using a combination of air gap, anti-scatter grid and beam collimation, and the success of some specialized imaging techniques, such as dual-energy and energy-subtraction methods, are particularly sensitive to achieving a low scatter-to-primary ratio (SPR)(2). In these situations, a simple and direct method to measure the SPR (also called the scatter ratio) at selected locations in a phantom image and under a wide range of conditions is required for several reasons including experimental validation of model predictions, to determine effectiveness of an anti-scatter grid, or to determine whether measured signal and noise are close to theoretical expectations.

Scatter estimation and correction has long been an important consideration in CT and cone-beam CT. Sun and Star-Lack developed an effective semi-empirical model validated by Monte Cario methods to remove scatter from projection measurements. Kermani and Feghhi describe a beam-modulating approach for high- energy industrial radiography. Computational methods. using Monte Carlo and artificial intelligence can be very effective but require expertise in those methods (3-8). None of these approaches negate the need for direct measurement in many cases.

The first direct measurements of scatter and glare (9-10) used beam-stop discs of vari- ous diameters and extrapolation to a zero-diameter disc (11). developed a method to measure SPR in mammography using a beam-blocking edge such as the tungsten edge often used to measure the modu- lation transfer function (MTF) to avoid the need for multiple discs and measurements (12,13). Their method is appropriate when scatter is constrained to half the beam width, a condition we call scatter equilibrium, and was validated using the Seibert method.

We build on the Cooper approach by using a nor- malized and over-sampled edge profile (14-16) and show it provides three primary extensions to the Cooper approach: (1) it does not require scatter equilibrium, nor a uniform phantom, making it appropriate for large air gaps, anthropomorphic phantoms and radio- graphic applications other than mammography; (2) it enables the use of a smaller beam and

---

*Corresponding author: Department of Mathematics, Ardabil Branch, Islamic Azad University, Ardabil, Iran.

E-mail address: Mehdi.fazli.s@gmail.com (Mehdi Fazli).

region of interest (ROI) for the analysis, and (3) it is tolerant of edge-alignment errors. We show that for the spe- cial case of scatter equilibrium with a uniform water phantom, resulting in shift-invariant scatter, it can also be used to determine the scatter line-spread function (LSF) and characteristic function in the Fourier domain.

Our method uses a Fourier analysis to separate broad scatter tails measured in edge images in the spatial domain from the transmitted primary beam. Although the Fourier transform (FT) is used throughout, we provide a detailed theoretical analysis to show that while linear image data is required, the SPR is correctly determined from the low-frequency drop (LFD) in the Fourier characteristic function even when scatter equilibrium is not achieved or scatter is shifting variant.

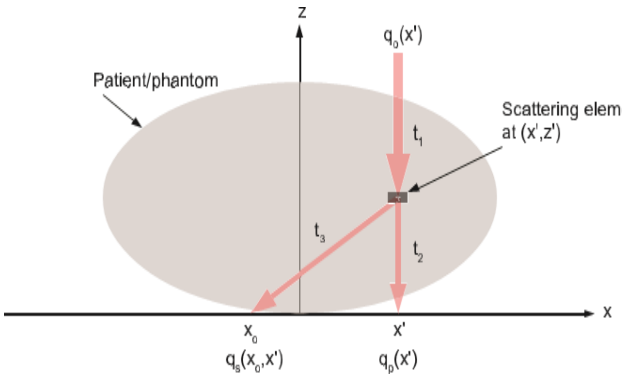

Figure.1. Illustration of scatter generated in a nonuniform phantom (or patient), showing scatter generated at position x′ and depth z′ in the phantom arriving at xo on the detector, where qo(x) is the distribution of photons incident on the phantom, qp(x) is the distribution of primary photons transmitted through the phantom and incident on the detector, and qs(x) is the resulting distribution of scatter. Terms t1, t2, and t3 are transmission factors in the segments as illustrated.

2. Theory of LFD Method

Our description of scatter is illustrated in Figure 1 where x is the direction across a one-dimensional detector and z is the perpendicular depth into a nonuniform phantom (or patient). One-dimensional detector geometry (x) is used for simplicity but the same results are obtained if a two-dimensional geometry (x, y) is used. This model is equivalent to that used by Sun and Star-Lack (3). Scatter distribution received at x from a narrow beam of width Δ_x at $x = x'$ is given by $q_s(\mathrm{x}, \mathrm{x}')$ where

$$q_s(x,x') = \int q_0(x')\,\Delta_X t_1(x',z')c(x',z')g(x,x',z')dz' \quad (1)$$

and where $q_0(x)[mm^{-1}]$ is the distribution of photons incident on the phantom, $c(x',z')[mm^{-1}]$ describes the probability of generating scatter per primary photon and unit distance z at (x',z') , $g(x,x',z')[mm^{-1}]$ describes the probability density scatter generated at (x',z') is received at x on the detector, and t_1, t_2 and t_3 are transmission factors as illustrated. The transmitted primary beam $q_P(x')$ can be expressed as

$$q_P(x') = q_0(x')t_1(x',z')t_2(x',z') \qquad (2)$$

for any z', and solving for scatter at $X = X_0$ gives

$$\begin{aligned} q_s(X,\acute{X})\big|_{X=X_0} &= q_P(\acute{X})\Delta_X \int c(\acute{X},\acute{Z})g(X,\acute{X},\acute{Z})/t_2(\acute{X},\acute{Z})d\acute{Z}\big|_{X=X_0} \\ &= \quad q_P(\acute{X})\Delta_X\alpha(\acute{X})s_e(X,\acute{X})\big|_{X=X_0} \qquad (3) \end{aligned}$$

The product αs_e represents the effective value of the product $cg\,/\,t_2$ from the integral along z through the nonuniform phantom and depends on many factors including phantom shape, composition, and density. The product gives the scatter distribution, relative to transmitted primary, coming from the narrow beam at x', and s_e is defined to have unity area for any x'.

Since we are solving for scatter at $x = x_o$ only, we can substitute $s_e(x,x') = s_{x_0}(x_0 - x')$. Integrating over all

$$q_s(X)|_{X=X_0} = \int q_P(\acute{X})\alpha(\acute{X})s_{X_0}(X-\acute{X})d\acute{X}\big|_{X=X_0} \qquad (4)$$

This is recognized as being a convolution integral evaluated at $x = x_o$:

$$q_s(X)|_{X=X_0} = [\alpha(X)q_P(X)] * s_{X_0}(X)\big|_{X=X_0} \qquad (5)$$

Equation (5) does not imply a convolution-based linear and shift-invariant (LSI) model of scatter. Rather, it shows that scatter at $x = x_o$ from a nonuniform phantom and nonuniform primary beam can be expressed as a convolution of the transmitted primary, scaled by $\alpha(x)$, with the scatter function specific to $x = x_o$, and the result evaluated at $x = x_o$. Only for the special case of a uniform phantom, where $\alpha(x)$ is constant and the scatter function becomes a shift-invariant LSF, is scatter given by the convolution integral.

$$q_s(X) = \alpha q_P(X) * S(X) \qquad (6)$$

where α is therefore seen to correspond to the SPR for an infinitely-wide beam incident on an infinite scattering medium.

In this work we use the convolution-based description in Equation (5) and set $x_o = 0$ as the position we measure the SPR. Therefore, α and $s(x)$ must correspond to that position, and we show below that we do not need to know the shape of $s(x)$ provided it has unity area and width much greater than the detector LSF.

2.1. Convolution model of scatter

At the center of a primary beam of width b with scattering medium larger than b, scatter is given by expanding Equation (6) as.

$$q_s = \alpha \int_{-\infty}^{+\infty} q_P(\acute{X}) S\left(X - \acute{X}\right) d\acute{X}\Big|_{X=0} \qquad (7)$$

$$= \alpha q_P \int_{-b/2}^{b/2} \frac{q_P(\acute{X})}{q_P} S\left(\acute{X}\right) d\acute{X} \qquad (8)$$

$$= \alpha\beta q_P \qquad (9)$$

where $q_p = q_p(X)\big|_{X=0}$, and β is the integral of s(x) weighted by the incident beam profile. We say scatter| equilibrium is reached when $\beta = 1$ and the SPR, also called the scatter fraction, corresponds to that of an infinite beam and infinite scattering medium. In general, $\beta < 1$ and the measured scatter fraction corresponds to the product $\alpha\beta$, giving the scatter fraction at the center of a specified finite beam which generally decreases as beam width is reduced. This result does not require a uniform beam, but scatter is expressed relative to the primary beam at the edge position. The detector signal, d(x), is proportional to the sum of detected primary and scatter:

$$d(X) = k[q_P(X) + q_s(X)] * l(X) \qquad (10)$$

$$= kq_P(X) * [l(X) + \alpha s_X * l(X)] * s_{X_0}(X)\big|_{X=X_0} \qquad (11)$$

$$= kq_P(X) * p(X) \qquad (12)$$

where k is a constant of proportionality and the kernel p(x), having area 1 + α, describes detector blur and scatter as a convolution with the transmitted primary beam.

The detector LSF, l(x), consists of a narrow peak, lp(x), generally having width much less than a millimeter, and sometimes a small broad base from detector glare, lg(x):

$$l(x) = (1 - \gamma)l_p(x) + \gamma l_g(x) \qquad (13)$$

where γ is the glare fraction. The kernel *p*(*x*) is therefore

$$p(x) = l(x) + \alpha s(x) * l(x) \quad (14)$$

$$(1 - \gamma)l_p(x) + p_b(x) \qquad (15)$$

which consists of the narrow peak $(1 - \gamma)lp(x)$ plus a broad base

$p_b(x) = \gamma l_g(x) + \alpha(1 - \gamma)s(x) * lp(x) + \alpha s(x) * l_g(x)$ resulting from scatter and glare. In the Fourier domain this corresponds to

$$P(u) = (1 - \gamma)T_p(u) + P_b(u) \qquad (16)$$

where $T_p(u)$ is the detector MTF excluding glare, $P_b(u) = \gamma Tg(u) + \alpha(1 - \gamma)S(u)Tp(u) + \alpha\gamma S(u)Tg(u)$ is a narrow peak at $u = 0$, and $S(u)$ is the FT of $s(x)$ and is also a narrow peak at $u = 0$. Separation of the narrow peak at $u = 0$ within $P(u)$ is key to our method and is used to distinguish the broad base resulting from glare and scatter from nonglare and non-scatter.

These relationships are illustrated in Figure 2. Uppercase variables indicate the FT of lower-case variables except for $T(u) = \mathscr{F}\{l(x)\}$. Zero-frequency values indicated by dashed lines on the Fourier vertical axis are known from the Fourier central-ordinate theorem.

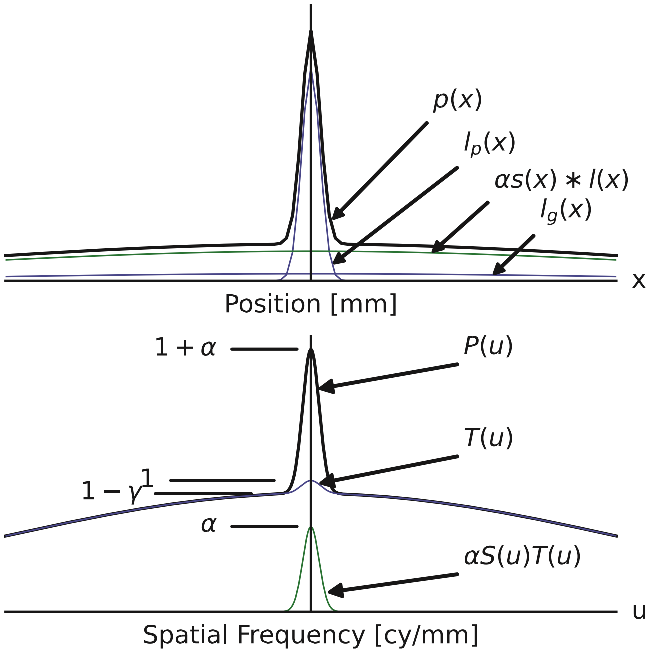

Figure.2. Illustration of p(x) = l(x) + αs(x) ∗ l(x) in the spatial domain (upper), corresponding to P(u) = T(u) + αS(u)T(u) in the spatial-frequency domain (lower). If all curves are symmetric about zero in the spatial domain, they are real-only in the Fourier domain.

2.2. Slanted-edge method

The slanted-edge method (12,14) has become the standard method to measure the detector LSF and MTF and is more accurate than other methods at low frequencies (17), important for this work. A radio-opaque edge is angled a few degrees (e.g., 1 to 15) from the pixel-column direction and all pixel values in the ROI are combined into a single 8× over-sampled edge profile which ensures negligible aliasing in the profile. Open-source code is available to assist with this calculation.

With no scattering medium present, the edge profile is differentiated to generate l(x) and the detector MTF is given by T(u). With the scattering medium present as illustrated in Figure 3, the FT gives P(u) which includes scatter. If the edge is placed at the same distance from the detector for each measurement, both T(u) and P(u) experience the same focal-spot blur.

2.3. Open and edge profiles

The open-field profile $d_o(x)$ for an infinite primary beam and scattering medium is given by

$$d_o(x) = kq_p(x) * p(x). \qquad (17)$$

Using Equation (9), the open-field profile value at the center of a finite beam is d_o given by

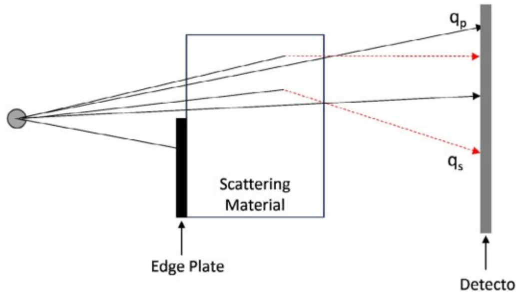

Figure.3. Schematic illustration of configuration used to obtain the scatter LSF from a water phantom. LSF, line-spread function.

$$d_0 = k \int_{-\infty}^{+\infty} q_P(\acute{X}) p\left(X - \acute{X}\right) d\acute{X} \qquad (18)$$

$$= k \int_{-b/2}^{b/2} q_P(\acute{X}) \left[l\left(X - \acute{X}\right) + \alpha s\left(X - \acute{X}\right)\right] d\acute{X} \qquad (19)$$

$$= kq_0[1 + \alpha\beta] \qquad (20)$$

With the edge plate in place, the edge-image profile $q_e(x)$ is given by

$$q_e(x) = k\left[p_q(x)H(x)\right] * p(x) \qquad (21)$$

where $H(x)$ is the Heaviside function. Our objective is to determine the product $\alpha\beta$, the scatter ratio from a finite beam, and $s(x)$, from measured open and edge-image profiles $d_o(x)$ and $d_e(x)$.

We have not placed any restriction on the beam profile $q_p(x)$, and some nonuniformity is expected from Heel effect and beam divergence. Although bright-field calibrations are used to accommodate variations in beam profile and pixel-gains, the actual profile generally remains inaccessible to the user. We therefore explicitly *require* normalization of an average edge image by an average open-field image (after subtracting an average dark image from each) acquired under identical conditions but without the edge plate. This gives $e(x) = d_e(x)/d_o(x)$ where $d_e(x)$ and $d_o(x)$ need not be bright-field corrected but the detector must have a linear response such that pixel value is proportional to exposure. The following simulations use a primary beam with maximum width 400 mm and off-centered 30% increase due to Heel effect as illustrated in Figure 4, although a variation of more than 15% was never seen in any experimental work.

These steps are illustrated in Figure 5 for a beam of width b = 200 mm and narrow and wide scatter LSFs σ_s = 5 and 50 mm in left and right columns, respectively. Open and edge profiles are shown in (b) and (c), and the normalized edge profile $e(x)$ in (d). Scatter equilibrium is achieved if $e(x)$ reaches 0 and 1 in attenuated and unattenuated limits, respectively. Profiles are determined only within an ROI of width r = 100 mm within the beam as illustrated in (e) and (f) for $e_r(x)$ and $\acute{e}_r(x)$. Additionally, the effect of the nonuniform beams which do not achieve scatter equilibrium is evaluated in the frequency domain as shown in Figure 6, and described in detail in the appendix.

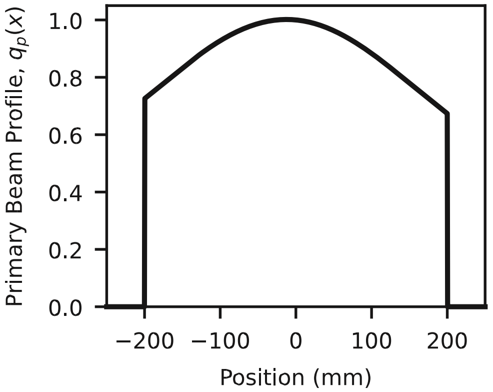

Figure.4. Simulated primary-beam profile with a width of 200 mm and approximately 30% Heel effect.

2.4. Scatter

Using the quotient rule,

$$\acute{e}_r(x) = \frac{\acute{d}_e(x)}{d_0(x)} - \frac{\acute{d}_0(x)}{d_0(x)} e(x) \qquad (22)$$

for $|x| < r / 2$ where

$$\acute{d}_0(x) = k\acute{q}_p(x) * p(x) \qquad (23)$$

$$\acute{d}_e(x) = k\left[\acute{q}_p(x)H(x)\right] * p(x) + kq_p p(x) \qquad (24)$$

and we used the product rule of differentiation and the convolution property

$$\frac{\partial}{\partial \mathrm{x}}[a(x) * b(x)] = a'(x) * b(x).$$

In the appendix we show that Equation (22) can be simplified to

$$\acute{e}_r(x) = \frac{1 - \gamma}{1 + \alpha\beta} l_p(x) + \epsilon(x) \qquad (25)$$

where, similar to $s(x)$, $\epsilon(x)$ describes a function we know little about other than it is very broad (such as a very wide Gaussian function), and that it therefore contributes only a narrow peak at $u = 0$ in the FT of $e'r(x)$.

2.5. Scatter

2.5.1. Spatial-domain analysis

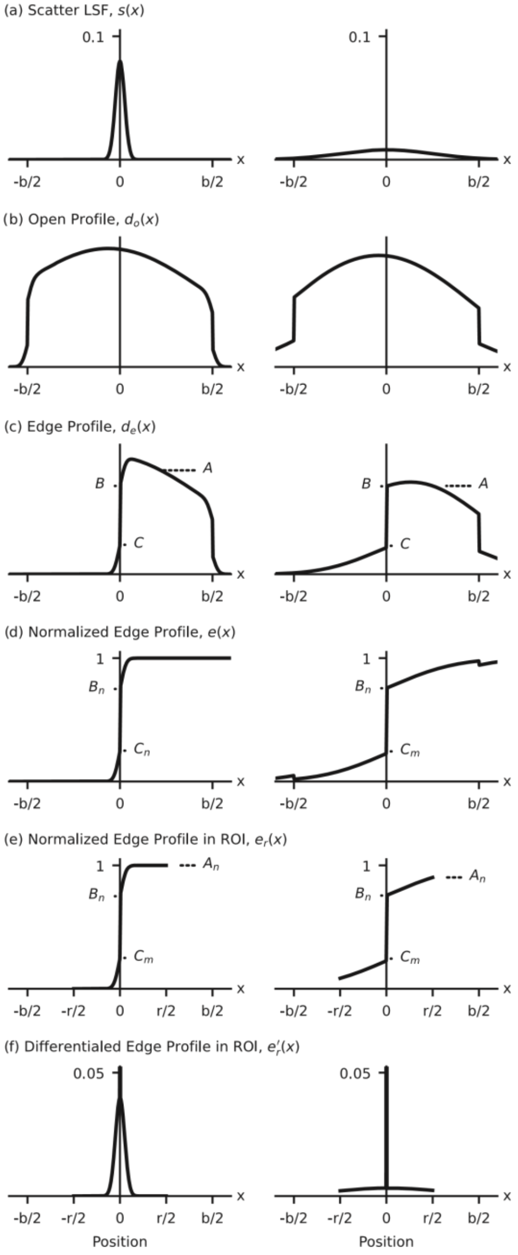

Figure.5. Illustration of steps required to measure scatter fraction for narrow and wide scatter LSFs where scatter equilibrium is achieved and not achieved, in left and right columns, respectively. The edge profile $d_e(x)$ is normalized by the open profile $d_o(x)$ to create the edge function $e(x)$ and evaluated over an ROI having width r and differentiated to give $e_r'(x)$. Curves were calculated as described in the theory section. LSFs, line-spread function; ROI, region of interest.

A connection with the Cooper method (11) is made by identifying the key positions they use on the edge profile in the spatial domain as identified in Figure 5. At position B, $d_e(x)$ is given by

$$d_{e_B} = k\int_0^{b/2} q_P(\acute{X})\, p(X-\acute{X})\, d\acute{X} = kq_p\left[1+\frac{\alpha\beta}{2}+\frac{\gamma}{2}\right] \qquad (26)$$

for a uniform beam. Similarly,

$$d_{e_c} = kq_p\left[\frac{\alpha\beta}{2}+\frac{\gamma}{2}\right] \qquad (27)$$

On the normalized-edge profile, these correspond to:

$$e_B = \frac{d_{e_B}}{d_{o_A}} = \frac{1+\frac{\alpha\beta}{2}+\frac{\gamma}{2}}{1+\alpha\beta} \qquad (28)$$

$$e_C = \frac{d_{e_C}}{d_{o_A}} = \frac{\frac{\alpha\beta}{2}+\frac{\gamma}{2}}{1+\alpha\beta} \qquad (29)$$

$$e_B - e_C = \frac{\left[1+\frac{\alpha\beta}{2}+\frac{\gamma}{2}\right]-\left[\frac{\alpha\beta}{2}+\frac{\gamma}{2}\right]}{1+\alpha\beta} = \frac{1}{1+\alpha\beta} \qquad (30)$$

$$\alpha\beta = \frac{1}{e_B - e_C} - 1 \qquad (31)$$

This result is similar to the Cooper SPR, although as a consequence of normalizing the edge profile by the open profile, Equation (31) is valid even when scatter equilibrium is not achieved.

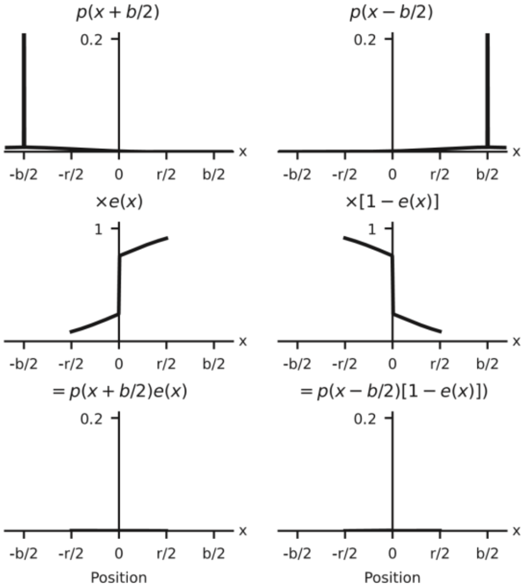

Figure.6. Illustration of terms in third and fourth lines of Equation (A3) corresponding to the right-hand column of Figure 5. Even when scatter equilibrium is not achieved (as illustrated), the contribution (bottom) consists of a slowly-varying base, contributing only low-frequency structure to $\acute{e}_r(x)$.

Quantum noise and rounded corners in edge profiles can make it difficult to determine these points accurately from the edge profiles in Figure 5c. In addition, our analysis shows it is not the corner values we require, but values where the near-vertical edge first meets scatter contributions. In the next section we describe a Fourier approach to determine the scatter fraction $\alpha\beta$, and scatter LSF when scatter equilibrium is achieved.

2.5.2. Fourier-domain analysis

The FT of $\acute{e}_r(x)$ in Equation (25) is

$$\mathcal{F}\{\acute{e}_r(x)\} = \acute{E}_r(u) = \frac{1-\gamma}{1+\alpha\beta} T_p(u) + \Delta(u) \tag{32}$$

$$= \acute{E}_p(u) + \Delta(u). \tag{33}$$

The first term, $\acute{E}_p(u)$, is proportional to $T_p(u)$, the optical transfer function excluding any LFD caused by glare and equal to unity at zero frequency. The second term, $\Delta(u)$, is a narrow peak at $u = 0$ with a height and area we do not know accurately, and importantly, do not need to know. These are illustrated in Figure 8, where the zero-frequency value $\acute{E}_p(u)|_{u=0}$ is equal to the shoulder height of $E_r'(u)$, indicated as L. By measuring the LFD value L, the scatter ratio is determined as

$$SPR = \alpha\beta \frac{(1-\gamma)T_p(u)}{\acute{E}_p(u)} - 1 \tag{34}$$

$$= \frac{1-\gamma}{L} - 1 \tag{35}$$

where γ is determined separately from a measurement of the detector MTF (without scatter). A key strength of our normalized-edge approach is that the terms we do not know accurately are all contained within $\Delta(u)$, which we know is a sharp peak at $u = 0$ and therefore does not contribute to the SPR in Equation (35). In the limit of no scatter, $L \rightarrow 1 - \gamma$ and $SPR \rightarrow 0$.

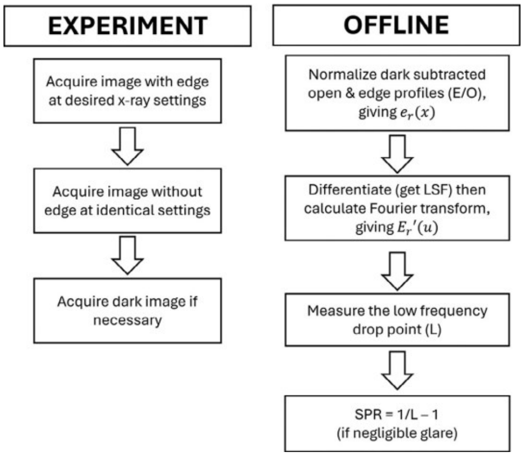

Figure.7. Schematic of experiment and offline calculation to determine the SPR using the LFD method, assuming negligible detector glare. This process must be repeated without the scattering medium if an estimate of detector glare is desired. LFD, low-frequency drop; SPR, scatter-to-primary ratio.

2.6. Experimental implementation

A flow diagram describing an implementation of the LFD method is illustrated in Figure 7. If detector glare is not negligible, the glare fraction γ in Equation (35) must be determined from the detector MTF measured without a scatter phantom.

2.7. Scatter LSF

When scatter equilibrium is achieved ($\beta = 1$) with a uniform primary beam, Equation (A3) reduces to

$$\acute{e}_r(x) \approx \frac{l(x) + \alpha s(x) * l(x)}{[1 + \alpha]} \tag{36}$$

and therefore

$$S(u) \approx \frac{1}{\alpha}\left[[1 + \alpha]\frac{\mathcal{F}\{\acute{e}_r(x)\}}{T(u)} - 1\right] \tag{37}$$

After measuring $T(u)$ separately with the scattering medium removed, and calculating α from Equation (35), $S(u)$ can be determined.

2.8. Simulation validation

A simulation of the scatter model was used to confirm our approximation that all terms in $\Delta(u)$ contribute only to a narrow peak at $u = 0$ and that the scatter ratio can be determined without knowing other details of the shape of $\Delta(u)$. Figure 8 illustrates the edge profile and magnitude of the FT of the differentiated profile for scatter LSF widths $\sigma s = 10$, 100, and 1000 mm, $\alpha = 1$, b = 100, and r = 50 mm, and with $\alpha = 5$ in Figure 9. Dashed lines indicate the theoretical shoulder value for each test based on simulation parameters. Table 1 lists shoulder heights determined from the curves, and compares corresponding scatter ratios with values from the simulation. Excellent agreement is obtained in all cases, confirming that the scatter fraction can be determined from the shoulder height through Equation (35) without detailed knowledge of $\Delta(u)$ for these parameters.

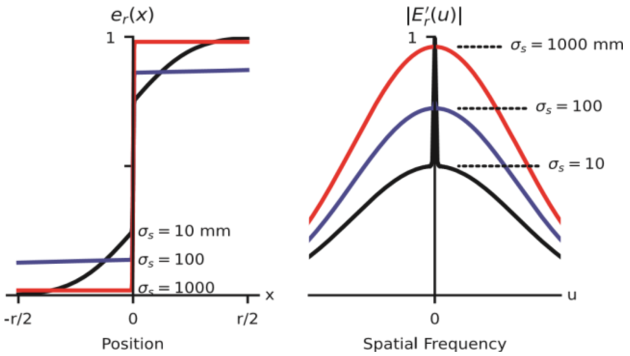

Figure.8. Illustration of er(x) and the magnitude of the FT of its derivative Er′(u) from the left column of Figure 5 for SPR $\alpha = 1$, beam width b = 100 mm, ROI r = 50 mm, and scatter

LSF widths σs = 10, 100, and 1000 mm. Dashed lines indicate theoretical scatter fractions $\alpha\beta$ which all agree accurately with the shoulder values L of Er′(u), even when scatter equilibrium is not achieved. FT, Fourier transform; LSF, line-spread function; ROI, region of interest; SPR, scatter-to-primary ratio.

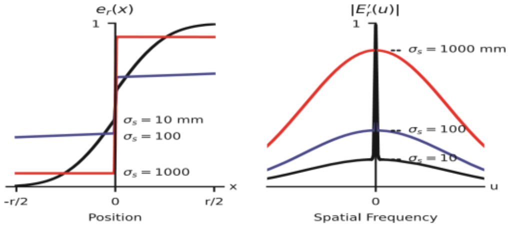

Figure.9. Similar to curves in Figure 8 with α = 5.

Table.1. Values of scatter ratios determined from the simulation agree with simulation parameters with a maximum error of 2%.

Scatter width, σs (mm)	Equilibrium scatter ratio, α	Beam width, b (mm)	β	Scatter ratio, $\alpha\beta$	Observed shoulder height, L (est ±0.03)	Observed scatter ratio, $\alpha\beta$	Error (%)
10	1	100	1.000	1.000	0.50	1.00	<1
100	1	100	0.383	0.383	0.72	0.381	<1
1000	1	100	0.035	0.040	0.96	0.040	<1
10	5	100	1.000	5.000	0.17	4.988	<1
100	5	100	0.383	1.916	0.34	1.907	<1
1000	5	100	0.040	0.200	0.84	0.198	1
10	1	100	1.000	1.000	0.50	1.000	<1
100	1	100	1.000	1.000	0.50	1.008	1
1000	1	100	1.000	1.000	0.49	1.024	2
50	1	100	1.000	1.000	0.51	0.976	2
50	1	200	0.955	0.955	0.52	0.938	2
50	1	400	0.683	0.683	0.60	0.684	<1

3. Experimental methods

Using the configuration shown in Figure 3 with a slanted 1/8-inch lead attenuator angled at 2.7 degrees, the following set of (unprocessed) images was acquired for every experimental condition:

1. scatter phantom + edge plate
2. scatter phantom only
3. edge only
4. open (no scatter phantom, no edge plate)
5. dark (required only if images are not dark corrected)

Edge and open profiles de(x) and do(x) were acquired and used to determine the normalized edge profile using the slanted-edge method (12). The normalized profile was differentiated and the FT determined as described in Figure 7. The zero-frequency value equals unity if (and only if) scatter equilibrium is obtained and it is important that the FT not be further normalized. If the detector is known to have little LFD due to glare, images 3 and 4 are not required.

3.1. Mammography

Scatter ratios were determined using both methods on a clinical mammography system (GE Pristina) using 2, 4, and 6 cm blocks of poly-methyl methacrylate (PMMA) placed on the detector cover at 24, 28, and 32 kV using 32 m As and a 0.3 mm molybdenum filter. Air gaps are measured from the beam-exit side of the phantom to the detector cover. The source-detector distance was 66 cm and the anti-scatter grid was in place.

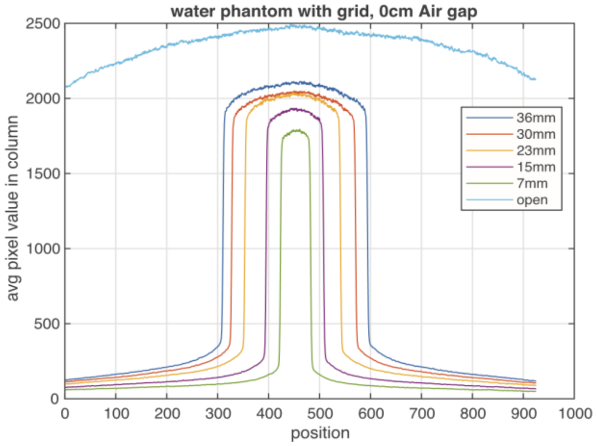

Figure.10. Profiles across a narrow beam using a uniform scatter phantom. Estimating scatter within the beam from scatter profiles outside the beam is error prone.

3.2. Radiography

Radiography data was acquired on a cardiac angiography system (Canon Alphenix). A 20-cm water-filled PMMA tank was placed in front of the detector and imaged using air gaps of 0, 10, 20, and 30 cm, both with and without an anti-scatter grid present, and at 60, 80, and 100 kV using 50–200 mA and 50 msec exposures. A 0.2-mm copper filter was placed in front of the beam. Results were obtained for a range of air gaps, lead-plate edge angles, ROI sizes, and edge positions. Beam collimation was used to ensure the beam was smaller than the scatter phantom. An anthropomorphic chest phantom was used to simulate nonuniform scatter conditions.

3.3. Thin-beam validation

The LFD method was validated by comparing with a thin-beam estimate as illustrated in Figures 12 and 13. The scatter component within the beam is estimated by interpolating the profile tails outside the beam, leading to an estimate of the primary component. Accuracy improves with a narrow beam, but results are susceptible to user error.

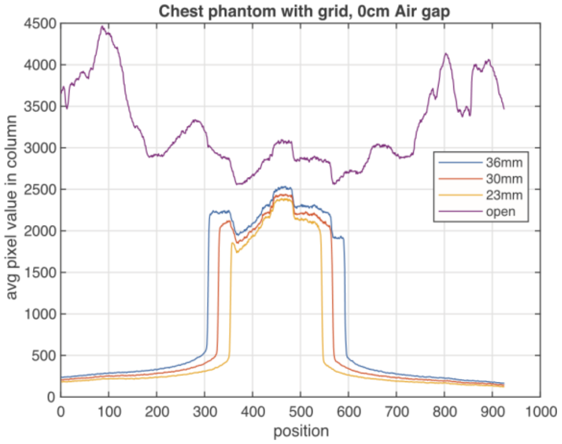

Figure.11. Profiles across narrow beams using a chest phantom.

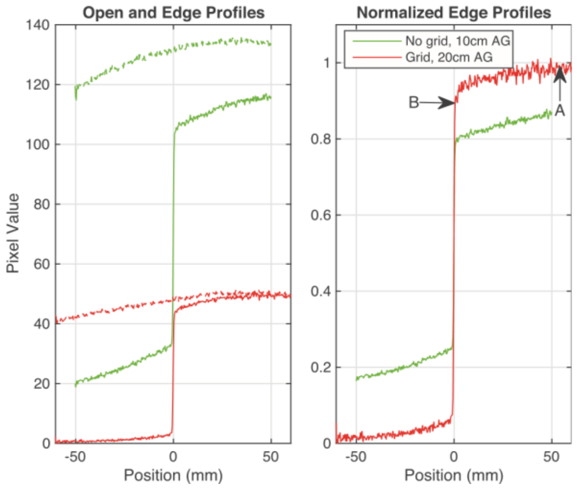

Figure.12. Left: Raw over-sampled profiles do(x) and de(x) acquired from open (dashed) and edge (solid) images, with (red) and without (green) scatter equilibrium. Right: Normalized edge profiles. Labels A and B correspond to regions of primary plus scatter and primary plus half scatter, respectively, as described by Cooper.

3.4. Edge response profile (ERP)

(Cooper) validation

The LFD method was further validated by comparison with the Cooper ERP method for conditions where scatter equilibrium was achieved. The Cooper SPR is given by:11

$$SPR_{cooper} = \frac{2(A - B)}{A - 2(A - B)} \qquad (38)$$

where A and B correspond to points A and B on the edge profiles in Figure 12. Equilibrium is achieved if profiles become flat near beam edges. Three repeated SPR measurements with a minimum wash-out period of 24 h were performed by the same observer for both methods to determine a precision estimate.

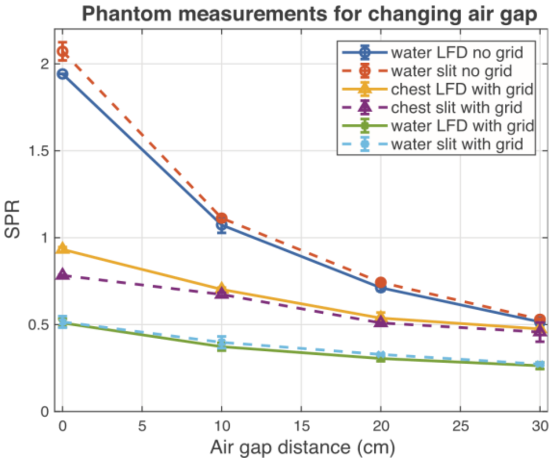

Figure.13. LFD method (solid) compared with the slit/narrow beam geometry measurement (dashed) for both a chest phantom with grid (triangle) and a water phantom with and without grid (cross and circle, respectively). Error bars represent standard deviation of three repeated measurements. LFD, low-frequency drop.

4. Results

Figure 12 (left) shows the over-sampled open and edge profiles for two sets of radiographic data at 60 kV, one that achieves scatter equilibrium (red curve, 20-cm air gap, and grid) and one that does not (green curve, 10cm air gap, and no grid). The corresponding normalized ERPs used in the SPR analysis are shown in Figure 12 (right) where the nonequilibrium data does not reach unity. In the latter case, the ERP method underestimates scatter since the vertical distance between points A and B is decreased.

Figure 13 shows agreement between the LFD and slit-beam methods for both a uniform water phantom and nonuniform chest phantom. Agreement is best for the more narrow beams where the slit-beam method is more accurate.

Results in Figure 14 show the mean calculated SPR value, with error-bars representing one standard deviation of three repeated measurements for each scenario. Scatter equilibrium was achieved for all mammography experiments and excellent agreement is shown between the LFD and Cooper ERP methods for all kilovoltage values and phantom thicknesses tested. These results cannot be compared directly with those of Cooper et al. due to experiment differences.

Figure 15 shows a comparison of LFD with ERP methods using radiographic data with 0, 10, and 20cm air gaps, as well as with and without an anti-scatter grid present (grid ratio 13). Error bars represent one standard deviation in repeated measurements and are smaller than plot symbols in some cases. The antichatter grid reduced the SPR by 78%, 75%, and 68% for 0, 10, and 20-cm air gaps, respectively. Without the anti-scatter grid, equilibrium was never achieved and the ERP method underestimated scatter as expected. Error bars are largest when using the ERP method without achieving equilibrium as points A and B are more difficult to identify. The detector had a measured glare fraction of less than 1% in all cases. When scatter equilibrium is achieved with use of the anti-scatter grid (dashed lines), the ERP method agreed with the LFD results.

Sensitivity of the SPR results to edge angle was tested at five angles and three air-gap distances using identical x-ray parameters as illustrated in Figure 16. In all cases, the SPR value remained constant within measurement precision, indicating that edge angle does not affect results over the range tested with the LFD method. Sensitivity to ROI size was tested using both ERP and LFD methods as shown in Figure 17. The LFD method showed no dependence on ROI size if greater than 15 mm, both with and without scatter equilibrium, consistent with the theoretical model.If less than 15 mm, the LFD value is difficult to determine in the spatial-frequency domain. The ERP method required a minimum ROI of approximately 30 mm (and scatter equilibrium).

When scatter equilibrium is achieved, the scatter MTF, $S(u)$, can be determined using Equation (37). Figure 18 illustrates measured $E_r'(u)$, $T(u)$ and $S(u)$ curves for 60 kV and 10 cm air gap and grid as an example ($\alpha = 0.19$ was determined from the LFD value in $E_r'(u)$). It shows the scatter MTF is essentially a narrow peak at $u = 0$ as expected, although the shape of the peak is under-sampled and noise in $|S(u)|$ is always positive.

5. Discussion

Normalizing the edge image by the open image allows the scatter ratio to be determined even when equilibrium is not achieved. Under nonequilibrium conditions, the measured frequency-domain data may exhibit a zero-frequency value of less than unity. This is expected and should **never** be re-normalized (i.e., forced to 1). Forcing the MTF to 1 at zero frequency artificially imposes that the area under the LSF equals 1, which is valid only when scatter equilibrium has been achieved. This assumption becomes incorrect if the scatter LSF tails extend beyond the measurement window.

The use of the over-sampled slanted-edge approach removes the need for precise alignment with detector pixel columns, improving robustness in practical measurements. Excellent agreement was observed between the LFD and edge response methods under conditions of scatter equilibrium. However, when scatter increases such as at higher kilovoltage values the equilibrium condition may no longer hold. This deviation is not always evident from the edge profiles alone, potentially leading to inaccurate SPR measurements if relying solely on the edge-profile method. Furthermore, the robustness of this method its insensitivity to ROI size and edge angle makes it practical for integration into routine quality assurance (QA) protocols in clinical settings.

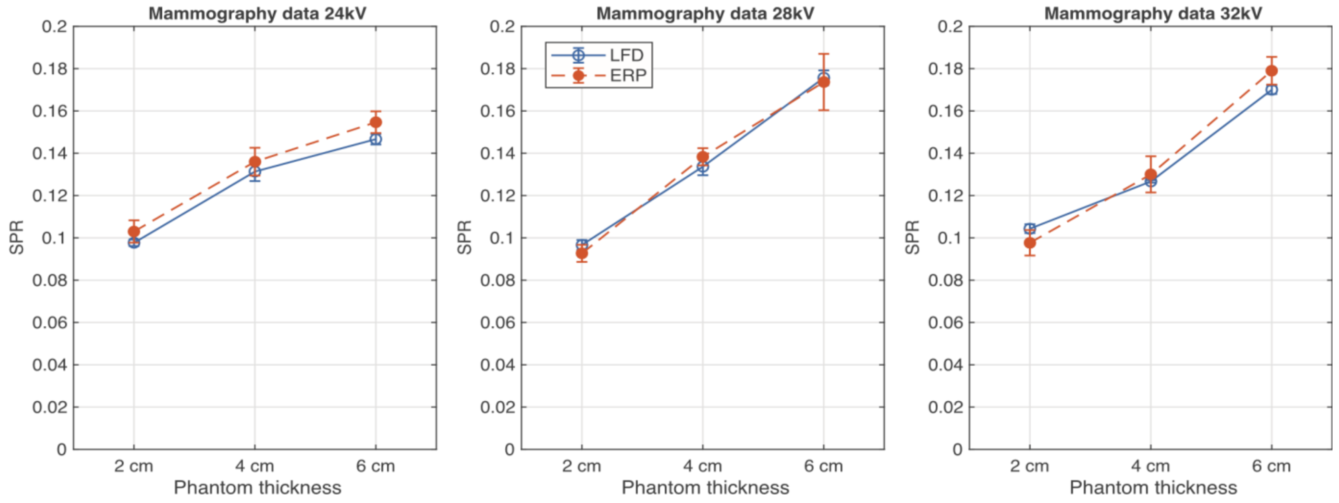

Figure.14. Good agreement is observed between LFD and Cooper ERP method for mammography with 2, 4, and 6 cm phantom thicknesses at 24, 26, and 32 kV. Both ERP (solid circle, dashed orange line) and LFD (hollow circle, solid blue line) calculation methods agree for all scenarios. ERP, edge response profile; LFD, low-frequency drop.

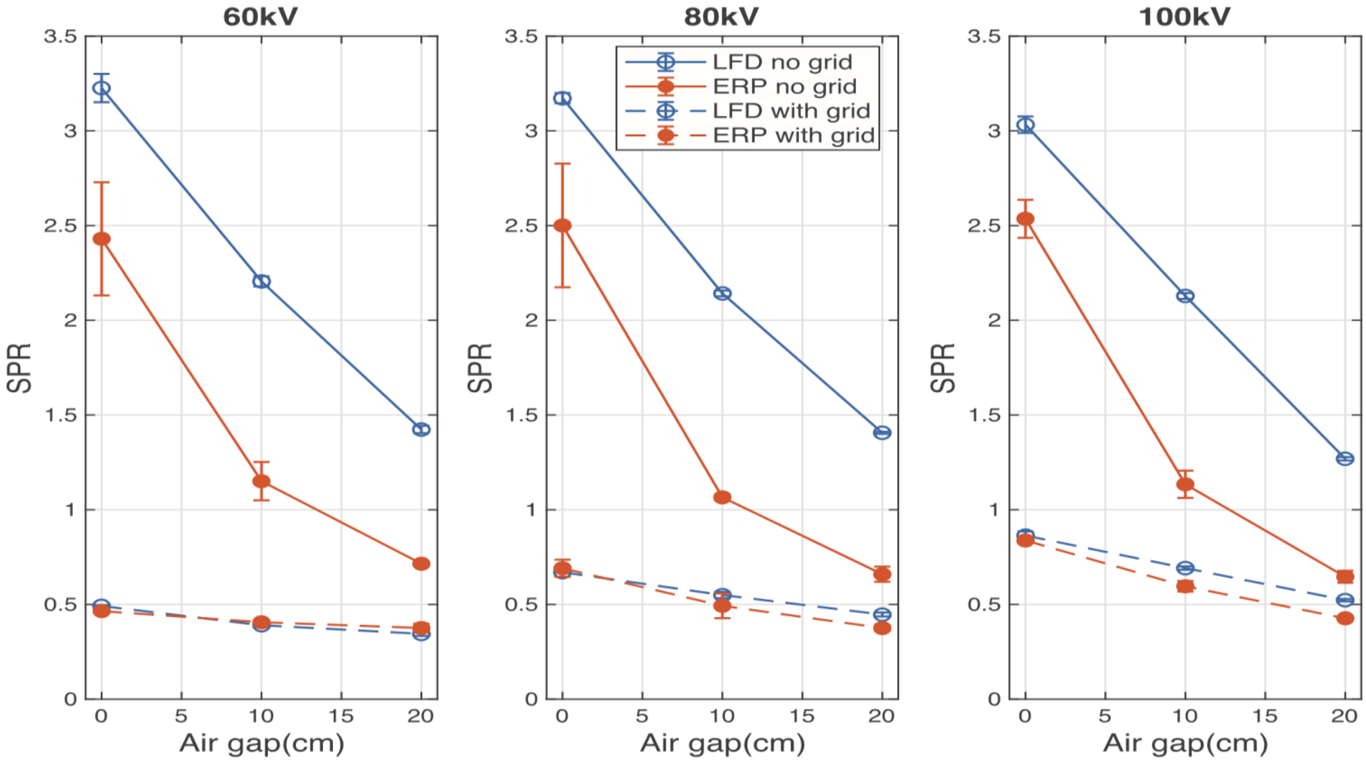

Figure.14. SPR data using ERP method (solid orange circle) and LFD method (hollow blue circle) for changing air gap with (dashed) and without (solid) anti-scatter grid using 60, 80, and 100 kV x-rays. ERP, edge response profile; LFD, low-frequency drop; SPR, scatter-to-primary ratio.

The thin-beam method offers an alternative direct measurement of scatter but is error prone due to difficulty interpolating the shape of the scatter profile in the primary beam in Figures 12 and 13, particularly with the larger beams and with the nonuniform phantom. This difficulty highlights the benefit of the LFD method for direct scatter measurements.

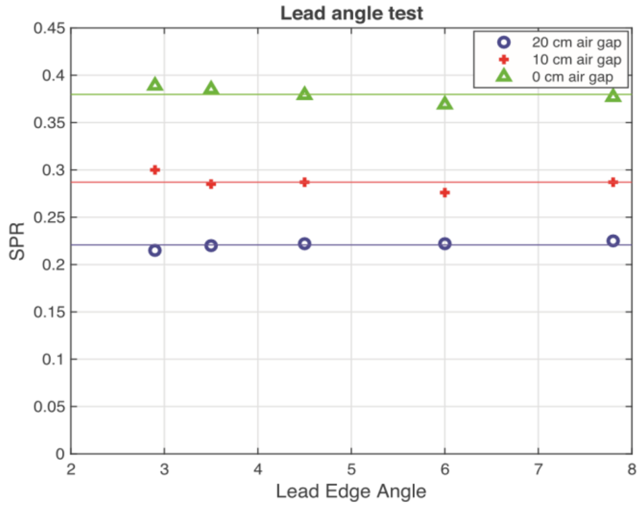

Figure.16. SPR values obtained with the LFD method as a function of edge angle using 0, 10, and 20 cm air gaps (60 kV with anti-scatter grid). LFD, low-frequency drop; SPR, scatter-to-primary ratio.

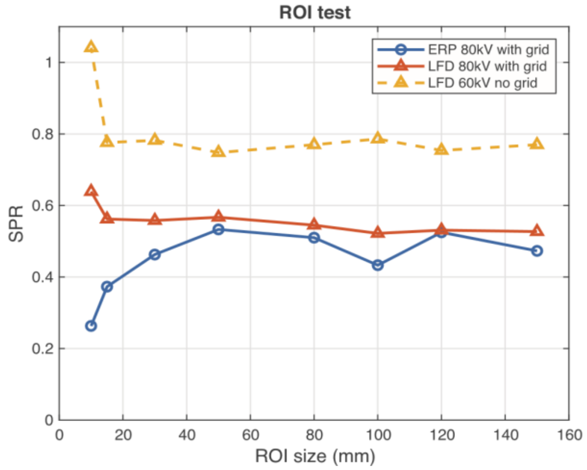

Figure.17. SPR values obtained as a function of ROI size. Solid lines correspond to scatter equilibrium conditions and dashed lines to nonequilibrium conditions. ROI, region of interest; SPR, scatter-to-primary ratio.

While the theoretical derivation of this method is rather obtuse, implementation is very straightforward since the SPR is determined from the shoulder height L of the FT of the differentiated edge profile as described by Equation (35). When there is no scatter medium present, the LFD method gives γ, the detector glare fraction. This measurement of γ may be important when measuring low scatter fractions and it is important to separate scatter from detector glare. In many cases, particularly with modern detectors, the glare fraction can be 1% or less which may have little impact on a measure of the scatter ratio and therefore an air scan may not be required.

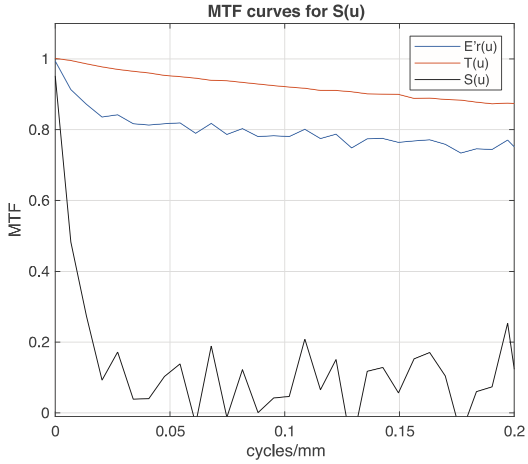

Figure.18. MTF curves for detector plus scatter Er′(u) in blue, detector T(u) in orange, and the calculated scatter MTF S(u) in black using 60 kV, 10 cm air gap, and calculated α = 0.19. MTF, modulation transfer function.

Limitations of this method include: (i) it requires access to raw, linear, and unprocessed image data, which is not always available to an end user; (ii) the scattering phantom must be larger than the x-ray beam; and (iii) the measured SPR is an average within the designated ROI in the direction parallel to the slanted edge.

6. Conclusion

We describe a Fourier-based LFD slanted-edge method of calculating the SPR given by Equation (35) and compare it with the Cooper et al. edge method and a simple thin-beam method. Similar to other methods, our approach requires the use of linear and dark-corrected image data. As a result of normalizing the edge profile with an open profile, we show theoretically and experimentally that the method works under a wide range of ROI sizes, edge angles, and unlike other methods does not require scatter equilibrium (beam can be smaller than scatter LSF width). Specific conclusions from this work include:

1. Use of the edge/open normalized profile eliminates the need for scatter equilibrium so that the beam can be much smaller than scatter width. This makes it appropriate for use in both mammography (where scatter equilibrium may be achieved) and radiography (where equilibrium is often not achieved).
2. The method is insensitive to variations in the edge angle (relative to image columns), is tolerant of a nonuniform primary beam, and requires only a 15 mm ROI in the normalized edge profile.
3. Results are consistent with a theoretical derivation of the method, and agree with the Cooper edge method when scatter equilibrium is achieved.

References

1. *Mazurov, A. and N. Potrakhov, Effect of scattered X-ray radiation on imaging quality and techniques for its suppression. Biomedical engineering, 2015. 48(5): p. 241-245.*
2. *Burton, C.S., J.R. Mayo, and I.A. Cunningham, Energy subtraction angiography is comparable to digital subtraction angiography in terms of iodine Rose SNR. Medical Physics, 2016. 43(11): p. 5925-5933.*
3. *Sun, M. and J. Star-Lack, Improved scatter correction using adaptive scatter kernel superposition. Physics in Medicine & Biology, 2010. 55(22): p. 6695.*
4. *Kermani, A. and S.A.H. Feghhi, Experimental Measurement of Scatter to Primary Ratio by Localized Primary Modulation in Industrial Computed Radiography. Journal of Nondestructive Evaluation, 2018. 37: p. 1-7.*
5. *Chan, H.P. and K. Doi, Physical characteristics of scattered radiation in diagnostic radiology: Monte Carlo simulation studies. Medical physics, 1985. 12(2): p. 152-165.*
6. *Zaidi, H. and M.R. Ay, Current status and new horizons in Monte Carlo simulation of X-ray CT scanners. Medical & biological engineering & computing, 2007. 45: p. 809-817.*
7. *Xiang, H., et al., A deep neural network for fast and accurate scatter estimation in quantitative SPECT/CT under challenging scatter conditions. European journal of nuclear medicine and molecular imaging, 2020. 47(13): p. 2956-2967.*
8. *Maier, J., et al., Deep scatter estimation (DSE): Accurate real-time scatter estimation for X-ray CT using a deep convolutional neural network. Journal of Nondestructive Evaluation, 2018. 37(3): p. 57.*
9. *Seibert, J.A., O. Nalcioglu, and W. Roeck, Characterization of the veiling glare PSF in x-ray image intensified fluoroscopy. Medical physics, 1984. 11(2): p. 172-179.*
10. *Maher, K., Comparison of scatter measurement techniques in digital fluoroscopy. Physics in Medicine & Biology, 1993. 38(12): p. 1977.*
11. *Cooper III, V.N., et al., An edge spread technique for measurement of the scatter-to-primary ratio in mammography. Medical physics, 2000. 27(5): p. 845-853.*
12. *Commission, I.E., Medical electrical equipment-Characteristics of digital X-ray imaging devices-Part 1-3: Determination of the detective quantum efficiency-Detectors used in dynamic imaging. IEC 62220-1-3, 2008.*
13. *Masaoka, K., Edge-based modulation transfer function measurement method using a variable oversampling ratio. Optics Express, 2021. 29(23): p. 37628-37638.*
14. *Judy, P.F., The line spread function and modulation transfer function of a computed tomographic scanner. Medical physics, 1976. 3(4): p. 233-236.*
15. *Samei, E., M.J. Flynn, and D.A. Reimann, A method for measuring the presampled MTF of digital radiographic systems using an edge test device. Medical physics, 1998. 25(1): p. 102-113.*
16. *Viallefont-Robinet, F., et al., Comparison of MTF measurements using edge method: towards reference data set. Optics express, 2018. 26(26): p. 33625-33648.*
17. *Cunningham, I. and B. Reid, Signal and noise in modulation transfer function determinations using the slit, wire, and edge techniques. Medical physics, 1992. 19(4): p. 1037-1044.*
18. *Samei, E., et al., Report of AAPM Task Group 162: Software for planar image quality metrology. Medical physics, 2018. 45(2): p. e32-e39.*
19. *Abbasi, B., et al., The effect of magnesium supplementation on primary insomnia in elderly: A double-blind placebo-controlled clinical trial. Journal of research in medical sciences: the official journal of Isfahan University of Medical Sciences, 2012. 17(12): p. 1161.*
20. *Shavisi, N., et al., Effect of PLA films containing propolis ethanolic extract, cellulose nanoparticle and Ziziphora clinopodioides essential oil on chemical, microbial and sensory properties of minced beef. Meat science, 2017. 124: p. 95-104.*